Consideration of artificial compressibility for explicit computational fluid dynamics simulation

kazuma, nagata
Interdisciplinary Graduate School of Engineering Sciences, Kyushu University

Ikegaya, Naoki
Interdisciplinary Graduate School of Engineering Sciences, Kyushu University

Tanimoto, Jun
Interdisciplinary Graduate School of Engineering Sciences, Kyushu University

https://hdl.handle.net/2324/4751322

1   Title: Consideration of artificial compressibility for explicit computational fluid dynamics
2   simulation
3
4
5   Authors:
6   K. Nagata[a], N. Ikegaya[a,b], and J. Tanimoto[a,b]
7
8
9   Affiliations:
10 [a] Interdisciplinary Graduate School of Engineering Sciences, Kyushu University, Japan
11 [b] Faculty of Engineering Sciences, Kyushu University, Japan
12
13
14 Corresponding author:
15 K. Nagata
16 Kasuga-koen 6-1, Kasuga-shi, Fukuoka 816-8580, Japan
17 +81-092-583-7644
18 nagata.kazuma@kyudai.jp

Abstract:

In this paper, we discuss the theoretical interpretation of the artificial compressibility method (ACM) to propose a new explicit method for the unsteady numerical simulation of fluid flow. The proposed method employs the compressible continuity and Navier–Stokes equations, which facilitates the replacement of pressure as one of the major variables with density, theoretically backed by virtual particle concept. This new concept justifies the theoretical treatment assuming the speed of sound in ACM as a model parameter determined by the grid system. More importantly, the present method realizes, in a fully explicit manner, the solving of a set of equations, which prevents the solving of the Poisson equation of pressure. The new method was validated and proven by comparing the results of two-dimensional cavity flow between the proposed method, conventional incompressible method, and the Lattice–Boltzmann method with varying Reynolds numbers (100, 1000, and 10000). The results of the proposed method agree well with conventional and reference data for both steady-state and unsteady-state conditions, although slight numerical oscillations were observed for the proposed method at a Reynolds number of 10000. Thus, the numerical validation assures that the proposed method is an explicit method based on a solid theoretical ground to be a new efficient simulation framework.

1. Introduction

Most computational fluid dynamics (CFD) simulations of air flow under low Mach conditions assume incompressible fluids because the compressibility of fluid is negligible for velocity fields. This assumption also means that the change in internal energy by dissipation and work by compression and expansion is not necessary to consider for such determination of the air flow. However, this also requires coupling the continuity and Navier–Stokes equations to determine the pressure p that inevitably requires solving the Poisson equation by an iterative numerical procedure, which accounts for the majority of computational load of such a conventional framework presuming 'incompressible fluid'.

To avoid solving the Poisson equation of p, several technical procedures have been proposed earlier. For example, Chorin [1] proposed a new algorithm known as the artificial compressibility method (ACM), in which some degree of artificial compressibility is considered despite dealing with an incompressible fluid. Technically, ACM replaces the speed of sound a with an arbitrary model parameter. This allows the method to solve the temporal evolution of p without an iteration process. Although ACM was originally aimed at solving a steady flow field of incompressible fluid with high numerical efficiency, some studies have reported that ACM can be applied for unsteady flow fields [2–4]. Additionally, modified ACMs have also been proposed as a numerically effective and stable method. Accordingly, Clausen [5] interpreted ACM as a compressible fluid with an isentropic process based on the theoretical equation of p. Additionally, they proposed an entropically damped artificial compressibility method (EDACM), which can reduce the acoustic wave propagation that causes temporal and spatial oscillations. EDACM replaced the temperature diffusion with pressure diffusion to reduce unfavorable oscillations in p and velocity $\boldsymbol{u}$. Ansumali et al. [6] proposed the kinetically reduced local Navier–Stokes equations (KRLNS), which establishes the simplified the pressure equation based on the grand potential instead of the entropy as the suitable thermodynamic potential. Borok et al. [7] conduct numerical simulations of two-dimensional cavity flow and two-dimensional Taylor-Green vortex flow to compare the results of the KRLNS and ACM. In addition, Toutant [8] proposed the general pressure equation (GPE), which the pressure equation is derived by the budget equation of the enthalpy, and compared them [9]. In the field of marine engineering, the technical approach of compressible CFD methods is also studied. For example, Bigay et al. [10] proposed a weakly-compressible cartesian hydrodynamic (WCCH) solver, which the pressure equation is based on the polytropic equation of state. All of these methods have the Eulerian governing equations such as Navier–Stokes equations, which means they describe the fluid motion on the macroscopic scale. On the other hand, the Lattice–Boltzmann method (LBM) [11] has been focused in various wind engineering fields. It solves the lattice Boltzmann equation, which means that it describes the flow motion on the mesoscopic scale. He et al. [12] compared LBM and ACM in detail to consider the relationship between them.

However, as mentioned above, several CFD methods have been proposed, we focus on ACM and EDACM in this study. Although these precursors successfully proved that their artificial compressible framework is applicable in solving incompressible fluid flows explicitly, the speed of sound a is determined by the arbitrary model parameter. Alternatively, these methods must be understood as technical procedures to solve problems regarding incompressible fluids numerically with an artificial parameter. As a result, both ACM and EDACM require the quantification of artificial parameter in numerical procedures, as reported in previous studies [13–17].

Motivated by the above background, we report a theoretical consideration accounting for incompressible fluids into an unsteady simulation framework, presuming a fully explicit method wherein a new idea relying on the virtual particle concept is introduced. The virtual

88 particles are conceptually ideal, that are introduced in the LBM; however, the proposed
89 method still retains the Eulerian governing equations, namely, the continuity and Navier–
90 Stokes equations. The proposed method is compared with the conventional CFD method
91 (Simplified Marker-And Cell method, or SMAC) [18], LBM, and that employed in a previous
92 study by Ghia et al. [19] for a two-dimensional cavity flow to justify the applicability of the
93 proposed method, named as the explicit method with the virtual particle concept (EMV).
94   This study is organized as follows: the theoretical background of EMV is explained
95 in Section 2, the velocity fields of the cavity flow are discussed in Section 3, and the
96 conclusive remarks are provided in Section 4.

97   2. Theory
98   2.1 Governing equations
99   We start from the theoretical budget equations for a compressible fluid to consider
100   the physical interpretation of artificial compressibility approaches (e.g., ACM and EDACM).
101   The continuity and Navier–Stokes equations for a compressible fluid can be written as

$$\frac{\partial \rho}{\partial t} + u_j \frac{\partial \rho}{\partial x_j} = -\rho\theta, \tag{2.1.1}$$

$$\rho \frac{\partial u_i}{\partial t} + \rho u_j \frac{\partial u_i}{\partial x_j} = -\frac{\partial p}{\partial x_i} + \frac{\partial}{\partial x_j}\left(\lambda\theta\delta_{ij} + \mu e_{ij}\right). \tag{2.1.2}$$

102   Here, variables are defined as follows; t: time [s], x_i: the coordinate for the i-th direction
103   [m], u_i: the velocity for the i-th component [m/s], p: the pressure [Pa], ρ: the fluid density
104   [kg/m^3], μ: the dynamic viscosity [kg/ms], λ: the second dynamic viscosity [kg/ms], $e_{ij} =$
105   $(\partial u_j/\partial x_i + \partial u_i/\partial x_j)$: the velocity strain tensor, δ_{ij}: the Kronecker's delta, and $\theta =$
106   $\partial u_i/\partial x_i$: the divergence of the velocity.
107   For an ideal gas, where ρ can be expressed by two independent microstate variables,
108   p and temperature T, $\rho = \rho(p, T)$. Hence, the total derivative of ρ with respect to t gives
109   the equation of p as follows:

$$\frac{D\rho}{Dt} = \left(\frac{\partial\rho}{\partial p}\right)_T \frac{Dp}{Dt} + \left(\frac{\partial\rho}{\partial T}\right)_p \frac{DT}{Dt}. \tag{2.1.3}$$

110   Here, $D/Dt = \partial/\partial t + u_j\partial/\partial x_j$, and the suffix of T or p indicates the partial derivative
111   with fixing T or p, respectively. By employing the continuity equation, the budget equation
112   of internal energy, and the ideal gas equation ($p/\rho = RT$, where R is the gas constant
113   [J/kgK]), we obtain

$$\frac{Dp}{Dt} = (\gamma - 1)\left(k\frac{\partial^2 T}{\partial x_j \partial x_j} + \phi\right) - \gamma p\theta. \tag{2.1.4}$$

114   Here, k is the thermal conductivity [J/Kms], ϕ is the dissipation rate of the kinetic energy
115   of the fluid per volume [J/m^{3}s], and $\gamma = c_p/c_v$ is the ratio of the specific heat (c_p: the
116   specific heat with the isobaric condition [J/kgK], and c_v is the specific heat with isochoric
117   condition [J/kgK]).
118   We consider how Eq. (2.1.4) is expressed for isothermal, isentropic, and isochoric
119   conditions.
120   For an ideal gas, the internal energy budget equation is written as follows:

$$\rho c_v \frac{DT}{Dt} = k\frac{\partial^2 T}{\partial x_j \partial x_j} + \phi - p\theta. \tag{2.1.5}$$

121   The isothermal condition means that $DT/Dt = 0$ and $\partial T/\partial x_j = 0$; therefore, we obtain
122   $\phi = p\theta$, meaning that the entire reduction of kinetic energy owing to the dissipation, balances
123   with work, by the pressure and volume expansion. Because the speed of sound a is defined
124   as

$$a^2 = \frac{\partial p}{\partial \rho}, \tag{2.1.6}$$

125   we can rewrite Eq. (2.1.4) under isothermal conditions by substituting $\phi = p\theta$ and $a^2 =$
126   p/ρ as follows.

$$\frac{Dp}{Dt} = -p\theta = -a^2\rho\theta. \tag{2.1.7}$$

127   For an isentropic condition, the specific entropy s [J/kgK], expressed by

$$\rho T \frac{Ds}{Dt} = k\frac{\partial^2 T}{\partial x_j \partial x_j} + \phi, \tag{2.1.8}$$

128   is kept constant. Therefore, we obtained $Ds/Dt = 0$, or RHS=0. By substituting $a^2 = \gamma p/\rho$,
129   we obtain.

5

$$\frac{Dp}{Dt} = -\gamma p\theta = -a^2\rho\theta, \tag{2.1.9}$$

130   which is identical to Eq. (2.1.7).

131   Eqs. (2.1.7) and (2.1.9) are identical because both the isothermal and isentropic
132   conditions are categorized as barotropic flow, where $p = p(\rho)$. Therefore, the simple chain
133   rule $Dp/Dt = (D\rho/Dt)(dp/d\rho)$ gives the following p equation:

$$\frac{Dp}{Dt} = -a^2\rho\theta, \tag{2.1.10}$$

134   with Eq. (2.1.6). Therefore, the p equation for both barotropic conditions is identically
135   expressed by using a, ρ, and θ. Eq. (2.1.10) is considered to be employed as a basic
136   equation for the original ACM [1], although they have not mentioned the physical meaning of
137   the governing equation. We recall the interpretation of Eq. (2.1.10), with several assumptions
138   applied in the ACM in Section 2.2.1.

139   For the isochoric condition, we can assume that $D\rho/Dt = 0$ in Eq. (2.1.3). Hence,
140   we obtain,

$$T = \frac{\gamma}{\rho c_p(\gamma - 1)}p. \tag{2.1.11}$$

141   Substitution of Eq. (2.1.11) to Eq. (2.1.5) gives

$$\frac{Dp}{Dt} = \alpha\gamma\frac{\partial^2 p}{\partial x_j \partial x_j} + (\gamma - 1)\phi - \gamma p\theta. \tag{2.1.12}$$

142   Here, $\alpha = k/\rho c_p$ [m^2/s] is the thermal diffusivity. Eq. (2.1.12) is the original form of p in
143   the equation used in EDACM [5], although they did not mention their assumption as the
144   isochoric condition. Under this condition, a cannot be defined since $a^2 = \partial p/\partial\rho \to \infty$
145   theoretically. However, we nominally denote $p = a^2\rho$. By substituting a and taking the
146   condition of $a \to \infty$, we obtain

$$\lim_{a\to\infty}\rho\theta = \lim_{a\to\infty}\frac{1}{\gamma a^2}\left(\alpha\gamma\frac{\partial^2 p}{\partial x_j \partial x_j} + (\gamma - 1)\phi - \frac{Dp}{Dt}\right) = 0. \tag{2.1.13}$$

147   This means that the isochoric condition is identical with the incompressible assumption.

148   Based on the equations of p in Eq. (2.1.10) for the barotropic condition, and Eq.
149   (2.1.12) for the isochoric condition, we discuss the premise and assumptions used in ACM
150   and EDACM in the following section.

151

152   2.2 Artificial compressibility approach
153   2.2.1. ACM by Chorin (1967) [1]
154   The original ACM proposed by Chorin [1] employed the following two assumptions:
155   i) a substantial derivative of p can be expressed as $Dp/Dt \sim \partial p/\partial t$, and ii) a is a model
156   parameter (or artificial speed of sound) satisfying $p = a^2\rho$. These assumptions give the
157   following p equation:

$$\frac{\partial p}{\partial t} = -a^2\rho\theta. \tag{2.2.1}$$

158   Therefore, employing ACM indicates that the following set of equations is solved.

$$\frac{\partial\rho}{\partial t} = -\rho\theta, \tag{2.2.2}$$

$$\frac{\partial u_i}{\partial t} + u_j\frac{\partial u_i}{\partial x_j} = -\frac{a^2}{\rho}\frac{\partial\rho}{\partial x_i} + \frac{1}{\rho}\frac{\partial}{\partial x_j}(\lambda\theta\delta_{ij} + \mu e_{ij}). \tag{2.2.3}$$

159   According to these equations, we discuss the physical meaning and interpretation of
160   ACM. First, the conventional ACM is used as a numerical technique to solve an
161   incompressible flow problem under steady-state conditions with an arbitrary parameter a. As
162   seen, the difference in Eq. (2.1.1), and Eq. (2.2.2), the mass conservation cannot be satisfied
163   under the unsteady-state condition in ACM. Therefore, we have to interpret that Eq. (2.2.2)
164   satisfies the physical constraint of continuity only when $\partial\rho/\partial t = 0$. In other words,

165 extending the ACM for solving an unsteady flow development is not theoretically appropriate.
166 Alternatively, Eq. (2.2.1) is physically reasonable even under an unsteady state if the
167 advection term of p (i.e., $u_j \partial p / \partial x_j$) remains the same as Eq. (2.1.10) for both barotropic
168 flow conditions. This means that we should solve the set of equations in Eq. (2.1.10), and Eq.
169 (2.2.3) for the unsteady-state flow. Secondly, Clausen (2013) [5] explains that ACM is one of
170 the limitations with isentropic assumption; however, both isothermal and isentropic (i.e.,
171 barotropic conditions) give the same p equation as in Eq. (2.1.7), and Eq. (2.1.9). Therefore,
172 the conventional ACM must be interpreted as barotropic flow under the assumption of
173 $u_j \partial_j p = 0$. The last aspect is the selection of a. We can understand that its preferable to
174 replace the value of a by an artificial speed of sound, that's less than its realistic speed in
175 terms of numerical procedure for both ρ and u_i because the characteristic speeds of the
176 system are expressed as u_i and $u_i \pm a$ from the eigenvalues of the coefficient matrix of the
177 governing equations. However, the aforementioned derivation of the set of equations for the
178 ACM does not explain why we can assume a as an arbitral model parameter.
179
180 2.2.2. EDACM by Clausen (2013) [5]
181   Clausen (2013) [5] introduced EDACM as a method that minimizes the density
182 fluctuation. When $\rho = \rho(p, T)$, the total derivative of ρ is

$$d\rho = \left(\frac{\partial \rho}{\partial T}\right)_p dT + \left(\frac{\partial \rho}{\partial p}\right)_T dp. \tag{2.2.4}$$

183 If we assume that $d\rho \sim 0$ as employed in the EDACM, we obtain

$$dp = -\left(\frac{\partial \rho}{\partial T}\right)_p \left(\frac{\partial \rho}{\partial p}\right)_T^{-1} dT = \rho c_p \left(1 - \frac{1}{\gamma}\right) dT. \tag{2.2.5}$$

184 The integral of Eq. (2.2.5) leads to Eq. (2.1.11), meaning that the assumption in EDACM is
185 identical to the isochoric or incompressible condition, although Clausen (2013) [5] did not
186 mention this aspect. In addition, the EDACM assumes that i) $\phi = 0$, and ii) $a^2 = \gamma p / \rho$.
187 When these assumptions are applied to Eq. (2.1.12), the p equation in EDACM is written as

$$\frac{Dp}{Dt} = \alpha \gamma \frac{\partial^2 p}{\partial x_j \partial x_j} - a^2 \rho \theta. \tag{2.2.6}$$

188 Hence, applying EDACM indicates that the following set of equations is solved.

$$\frac{\partial \rho}{\partial t} + u_j \frac{\partial \rho}{\partial x_j} = -\rho\theta - \frac{\phi}{Tc_v}, \tag{2.2.7}$$

$$\frac{\partial u_i}{\partial t} + u_j \frac{\partial u_i}{\partial x_j} = -\frac{a^2}{\gamma\rho} \frac{\partial \rho}{\partial x_i} + \frac{1}{\rho} \frac{\partial}{\partial x_j} \left(\lambda\theta\delta_{ij} + \mu e_{ij}\right). \tag{2.2.8}$$

189   Similarly, the mass conservation is not achieved in EDACM because of the
190 difference in Eq. (2.2.7), and Eq. (2.2.1). Additionally, the physical interpretation of Eq.
191 (2.2.7) is not clear. Moreover, EDACM must be interpreted as an isochoric (incompressible)
192 condition because minimizing $d\rho$ is absolutely required. However, the condition is satisfied
193 only when $a^2 = \partial p / \partial \rho \to \infty$. Nonetheless, the parameter a appears in Eq. (2.2.8) as an
194 arbitrary model parameter. Furthermore, the derivation of equations for EDACM does not
195 explain why a can be a model parameter.
196   To summarize the problems in artificial compressible approach, firstly mass
197 conservation is not satisfied theoretically, and secondly the speed of sound a can be selected
198 as an arbitrary model parameter that is also not explained theoretically. We think that both
199 aspects are not critical issues in terms of solving the fluid dynamics numerically, based on
200 ACM and EDACM, as previous researchers have justified the accuracy of these methods by
201 comparing the conventional numerical method [4,14]. However, theoretical understanding is
202 required to reason, why these assumptions allow us to derive the fluid dynamics motion
203 numerically, based on artificial compressibility equation with parameter a.

204
205 2.3 Interpretation of parameter a
206 2.3.1. General theory of kinetic energy of gases
207   To provide a theoretical interpretation to assume a as the model parameter in ACM
208 and EDACM, we consider the fundamental definition of the pressure by molecule motions.
209 Given that a mono-atomic molecule i of n [mol] with mass m [kg/pcs], the velocity $\boldsymbol{q^i}$
210 [m/s], the total internal energy U [J] is

$$U = 0.5m\Sigma_i^{nN_A}\boldsymbol{q^i}^2 = 0.5mq_T^2nN_A, \tag{2.3.1}$$

211 where N_A is Avogadro number, by taking the summation of the total number of molecules
212 nN_A [pcs]. q_T is the root mean squared speed of molecules, or the thermal velocity, which is
213 written as

$$q_T^2 = \frac{1}{nN_A}\Sigma_i^{nN_A}\boldsymbol{q}_i^2 = \frac{\int_{-\infty}^{\infty}f(\boldsymbol{q})\boldsymbol{q}^2\,d\boldsymbol{q}}{\int_{-\infty}^{\infty}f(\boldsymbol{q})\,d\boldsymbol{q}}. \tag{2.3.2}$$

214 Here, $f(\boldsymbol{q})$ is the Maxwell distribution for molecules with respect to velocity $\boldsymbol{q}$ [m/s]. Eq.
215 (2.3.1) is also written as

$$U = \frac{0.5}{D}m\Sigma_i^{nN_A}q_x^i{}^2 \;\;(for\;D) = \begin{cases} 0.5m\Sigma_i^{nN_A}q_x^i{}^2 \;\;(for\;1D) \\ 0.5m\Sigma_i^{nN_A}\left(q_x^i{}^2 + q_y^i{}^2\right) \;\;(for\;2D) \\ 0.5m\Sigma_i^{nN_A}\left(q_x^i{}^2 + q_y^i{}^2 + q_z^i{}^2\right) \;\;(for\;3D) \end{cases}. \tag{2.3.3}$$

216 Because of the homogeneity of molecules in each direction for dimension D. Here, q_x^i, q_y^i
217 and q_z^i represent the velocity component in x, y, z and direction of $\boldsymbol{q^i}$, respectively.
218   Meanwhile since molecule motions are given by a change in momentum in one
219 direction per unit area:

$$p = m\Sigma_i^N q_x^i{}^2. \tag{2.3.4}$$

220 Here, N [pcs/m³] is the molecular density per unit volume ($=nN_A/\Omega$ [pcs/m³], where Ω [m³]
221 is the fluid volume). By multiplying Ω, we obtain

$$p\Omega = m\Sigma_i^{nN_A}q_x^i{}^2. \tag{2.3.5}$$

222 Therefore, the following relationship for U and p for D-dimensional gas can be obtained:

$$p\Omega = \frac{2U}{D} = \frac{mq_T^2nN_A}{D}. \tag{2.3.6}$$

223 We call Eq. (2.3.6) the general form of Bernoulli's theorem for D-dimensional gas. By
224 dividing Ω, p can be written as:

$$p = \rho\frac{q_T^2}{D}, \tag{2.3.7}$$

225 where $\rho = nN_Am/\Omega$ [kg/m³] is the total number of molecules multiplied by the mass per
226 volume. This indicates that pressure is given by thermal velocity q_T defined by the total
227 mean internal energy of molecules.
228
229 2.3.2. Explicit method with virtual particle concept (EMV)
230   On introduction of the concept of virtual particles, by grouping molecules of number
231 E, the particle will have a velocity $\boldsymbol{q}_v^i$, where i represents an index to express the i-th virtual
232 particle ($i = 1$ to nN_A/E). The virtual particle can move from one point to another, defined
233 by a lattice grid with uniform grid length of Δ during a representative time scale Δt. The
234 motion to diagonal neighboring grids, such as the length of $\sqrt{2}\Delta$ and $\sqrt{3}\Delta$, is also possible
235 depending on considering ultra-discretization, which means the discretization of the
236 dependent variables. In this context, velocity of the molecules is discretized as $\boldsymbol{c}_i$ ($i = 0$ to
237 M, where M is the number of discretized velocities). Examples of the lattice grid are given in
238 Appendix A1.

By following the definition and derivation of U and p based on the theory of kinetic energy of gases, we can define the internal energy U_v and pressure p_v by the virtual particles as follows:

$$U_v = 0.5 m_v \Sigma_i^{nN_A/E} \boldsymbol{q}_v^{i\,2} = 0.5 m_v q_{vT}^2 \frac{nN_A}{E} = 0.5 m q_{vT}^2 nN_A. \tag{2.3.8}$$

Here, $m_v = mE$ [kg] is the mass of virtual particle with E a molecule. The root mean squared velocity of the virtual particle, q_{vT}, is

$$q_{vT}^2 = \frac{E}{nN_A} \Sigma_i^{nN_A/E} \boldsymbol{q}_v^{i\,2} = \frac{\Sigma_{i=0}^M f_i \boldsymbol{c}_i^2}{\Sigma_{i=0}^M f_i}. \tag{2.3.9}$$

Here, f_i ($i = 0$ to M) is the distribution function of the virtual particle. f_i and $\boldsymbol{c}_i$ are determined once the lattice grid for the discretization is defined (please refer to Appendix A1). If we assume that the distribution of virtual particle is homogenous in each D direction, we obtain

$$U_v = \frac{0.5}{D} m_v \Sigma_i^{nN_A/E} q_{vx}^{i\,2}. \tag{2.3.10}$$

Here, q_{vx}^i represents the x-component of $\boldsymbol{q}_v^i$. The pressure p_v due to virtual particle motions is given by a change in the momentum in one direction per unit area as:

$$p_v = m_v \Sigma_i^{N/E} q_{vx}^{i\,2}. \tag{2.3.11}$$

Here, N/E [pcs/m³] is the virtual particle density per unit volume ($= nN_A/E\Omega$). By multiplying Ω, we obtain

$$p_v \Omega = m_v \Sigma_i^{nN_A/E} q_{vx}^{i\,2}. \tag{2.3.12}$$

Therefore, the following relationship is obtained for U_v and p_v for D dimensional flow:

$$p_v \Omega = \frac{2U_v}{D} = \frac{m_v q_{vT}^2 nN_A}{DE} = \frac{m q_{vT}^2 nN_A}{D}. \tag{2.3.13}$$

By dividing Eq. (2.3.13) by Ω,

$$p_v = \rho_v \frac{q_{vT}^2}{D} = \rho \frac{q_{vT}^2}{D}. \tag{2.3.14}$$

Here, $\rho_v = (m_v nN_A)/E\Omega = mnN_A/\Omega = \rho$ [kg/m³] is the fluid density. This is $\rho = \rho_v$ because the total mass does not change when the molecules or virtual particles are accounted for.

From Eqs. (2.3.8) and (2.3.14), the following relationships are obtained:

$$U_v = U \frac{q_{vT}^2}{q_T^2}, \tag{2.3.15}$$

$$p_v = p \frac{q_{vT}^2}{q_T^2}. \tag{2.3.16}$$

Therefore, U_v and p_v are smaller than those determined by kinematic energies of molecules. This is because the virtual particle is defined as a group of E molecules, indicating that internal energy within the group is not accounted for by U_v and p_v. When we denote these differences as ΔU_v and Δp_v, U and p are written as

$$U = U_v + \Delta U_v$$
$$= 0.5 m_v q_{vT}^2 \frac{nN_A}{E} + \Delta U_v, \tag{2.3.17}$$

$$p = p_v + \Delta p_v$$
$$= \frac{\rho q_{vT}^2}{D} + \Delta p_v. \tag{2.3.18}$$

This also gives,

$$\Delta p_v = \frac{2\Delta U_v}{\Omega D}. \tag{2.3.19}$$

If we can group E molecules such that $\Delta U_v/\Omega = Const.$ with respect to x_i, the pressure gradient term in the Navier–Stokes equation can be written as

9

$$\frac{\partial p}{\partial x_i} = \frac{\partial p_v}{\partial x_i} + \frac{\partial \Delta p_v}{\partial x_i} = \frac{\partial p_v}{\partial x_i}. \tag{2.3.20}$$

265 That allows us to replace p to p_v in the Navier–Stokes equations, indicating that the
266 pressure determined by all molecule motions is not necessary for calculating the macroscopic
267 fluid distributions.
268   The applicability of this concept may depend on how the group of E molecules is
269 defined, whereas the definition of grouping is very ambiguous because the selection of E
270 does not appear in the derived relationship in Eqs. (2.3.17)–(2.3.20). The virtual particle
271 concept being introduced is itself is identical to that of LBM; however, the present
272 explanation of the virtual particle concept gives a theoretical understanding that pressure due
273 to internal energy within the virtual particle is neglected in the LBM.
274   If we select a lattice grid, f_i and c_i in Eq. (2.3.9) are explicitly determined, and
275 therefore, we obtain the following expression for p_v (please refer to Appendix A2 for the
276 derivation).

$$p_v = \rho \frac{c^2}{3} = \frac{\rho}{3}\left(\frac{\Delta}{\Delta t}\right)^2. \tag{2.3.21}$$

277 This relationship is identical to the assumption that $a = \Delta/(\sqrt{3}\Delta t)$. Therefore, the concept of
278 a virtual particle justifies that speed of sound a, can be an artificial parameter, determined by
279 the grid system of a numerical simulation. However, a is not an arbitrary parameter that can
280 be empirically determined, but is one that is fixed by the grid system. By employing Eqs.
281 (2.1.2) and (2.3.21), we can get the final version of the Navier–Stokes equations of EMV as
282 follows;

$$\frac{\partial \rho u_i}{\partial t} + \frac{\partial \rho u_i u_j}{\partial x_j} = -\frac{1}{3}\left(\frac{\Delta}{\Delta t}\right)^2 \frac{\partial \rho}{\partial x_i} + \frac{\partial}{\partial x_j}\left(\lambda\theta\delta_{ij} + \mu e_{ij}\right). \tag{2.3.22}$$

283 As a result, we can solve u_i and ρ explicitly by Eqs. (2.1.1) and (2.3.22). Therefore, we
284 refer to this as the explicit method with virtual particle concept (EMV). The Mach number of
285 EMV is calculated by the following equation, which becomes larger than real;

$$Ma = \frac{V}{a} = \sqrt{3}V\left(\frac{\Delta t}{\Delta}\right) \tag{2.3.23}$$

286 Here, Ma is the Mach number [−] and V is the fluid velocity [m/s]. The justification for
287 introducing the virtual particle for reproducing the velocity fields of incompressible fluids is
288 discussed in Section 3.

289 3. Application to two-dimensional cavity flow
290 3.1 Numerical description
291   A two-dimensional cavity flow has been solved using the EMV, conventional CFD
292 (based on Simplified Marker and Cell, hereafter, denoted as SMAC [18]), and LBM.
293 Additionally, the results were compared with reference data by Ghia et al. [19], who
294 conducted direct numerical simulation based on coupled strongly implicit multigrid
295 (CSI-MG) method [20]. This section describes the basic numerical conditions employed in
296 these simulations.
297   Fig.1 and Table 1 show the schematic diagram of cavity and numerical conditions for
298 each case. We consider a simple two-dimensional cavity flow in which the side and bottom
299 walls are fixed and the top is specified as fixed velocity of $u_t = 1$m/s. μ is fixed as well, and
300 the width and height of the cavity denoted as H is determined by the Reynolds number
301 $Re = \rho_o u_t H / \mu$, where ρ_o is the initial air density since ρ changes with time in EMV and
302 LBM. Three conditions of Re number are employed: $Re = 100$, 1000, and 10000. Grid
303 numbers of 100^2, 150^2, and 250^2 are used, respectively, for each Re. A uniform grid
304 resolution $\Delta x = \Delta y = \Delta$ is applied in x and y directions for EMV, SMAC, and LBM.
305   The governing equations are discretized in a staggered grid system [21] for EMV and
306 SMAC. As for the temporal development, the first-order Euler scheme is adopted with $\Delta t =$
307 $C_o \Delta / u_t$ for SAMC and $\Delta t = C_0 \Delta / (u_t + a)$ for EMV and LBM. Here, C_o is the Courant
308 number. For SMAC method, $C_o = 0.25$, whereas $C_o = u_t \Delta t / \Delta + 1/\sqrt{3} \sim 0.83$ for EMV and
309 LBM in the present simulations. We employed the different Courant numbers in SMAC and
310 other methods because we employed the same Δt for all the simulations. The advection,
311 diffusion, and pressure terms are discretized by the second-order central scheme, whereas the
312 first-order upwind and total variation diminishing (TVD) scheme [22] are employed for
313 advection terms of continuity and Navier–Stokes equations when $Re = 10000$. This is
314 because the numerical oscillations cannot be reduced in the EMV with $Re = 10000$. It
315 should be noted that we were able to obtain the converged flow fields even though the
316 second-order central scheme was employed in the advection term in the explicit methods of
317 SMAC and EMV due to the molecular and numerical diffusion terms. The details of
318 discretization are given in Appendix A2. LBM employs a 2D9V (two-dimensional and
319 nine-discrete particle speeds) grid system with the BKG model [23] with collocation grids.
320
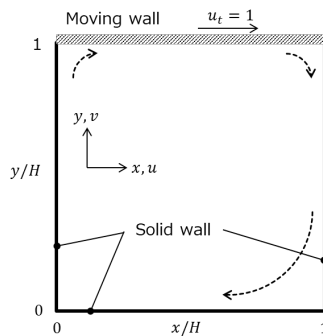
321
322 Fig.1 Schematic diagram of numerical domain.
323
324 Table 1. Numerical settings for compared simulations and reference data.

Method	Variables to be solved	Storage	Discretization Advection	Diffusion/Gradient
EMV ($Re = 100$, 1000)	u_i, ρ	1st - Euler	2nd - central	2nd - central
EMV ($Re = 10000$)	u_i, ρ	1st - Euler	1st-upwind (ρ) TVD (u_i)	2nd - central

11

SMAC	$u_i,\ p$	1st - Euler	2nd - central	2nd - central
LBM	f_i	-	-	-
Ghia et al. [19]	$u_i,\ p$	-	Khosla et al. [24]	2nd - central

3.2 Converged flow distribution

Fig. 2 shows snapshots of the streamlines and p distribution at $t = t_e$ for each Re number. Here, t_e represents the time when flow fields converge. p in EMV and LBM represent the values determined by ρ from distribution of Eq. (2.3.21). As can be seen in Fig. 2 (a–c) of $Re = 100$, three calculation methods show identical primary vortex as well as pressure distribution in a steady-state condition. Additionally, the secondary vortices shown at both bottom corners are also well captured for all three methods. When $Re = 1000$ in Fig. 2 (d–f), similar results can be seen; i.e., both primary and secondary vortices were well reproduced for each method. In the case of $Re = 10000$, the EMV in Fig. 2 (g) reproduces the primary vortex and vortices in the bottom-right corner as those in SMAC in Fig.2 (h). Additionally, subsidiary vortices in the bottom-right and left-top corners are seemingly identical. In contrast, slight differences in the vortex shapes near the left-bottom corner can be observed. Although the LBM can capture the primary vortex consistent with the other two methods, the shapes of subsidiary vortices differ from those of EMV or SMAC. This result means that both the EMV and LBM employed identical concepts for determining p; however, the reproduced flow field slightly differed from each other. In contrast, EMV and SMAC show significantly similar flow patterns regardless of the difference in the governing equations.

Regarding numerical stability for each simulation, a slight numerical oscillation can be seen at pressure distribution of $Re = 10000$ near the right wall ($x/H \sim 0.9, y/H \sim 0.5$) only in EMV (Fig.2 (g)), although both SMAC (Fig.2 (h)) and LBM (Fig.2 (i)) do not show any unnatural fluctuations. This is confirmed by exploring time evolutions of u and p at several points, despite not showed in this paper. The dominant frequency of these oscillations in EMV are much higher frequency than the frequency of propagations of the sound waves. Thus, we concluded that this oscillation is because EMV solves the governing equations explicitly, whereas SMAC employs iterative simulation by solving the Poisson equation of p.

The velocity profiles of the EMV are compared with those of SMAC, LBM, and direct numerical simulation (DNS) results (Ghia et al. (1982) [19]) in Fig. 3. The vertical profiles of u and horizontal profiles of v are taken at x/H=0.5 and y/H=0.5, respectively. Both velocity components are normalized by u_t. As can be seen in Figs. 3 (a) and (b), the results of EMV show profiles identical to those of SMAC and Ghia et al. (1982) at $Re = 100$ and 1000, indicating that EMV can reproduce the flow fields, similar to the conventional method, even though explicit numerical method is employed.

On the other hand, the profile of EMV is underestimated by approximately 15% at maximum as compared with those of SMAC and DNS, $Re = 10000$ as shown in Fig. 3 (c). The difference is the most significant at the peaks of u and v near each wall. Furthermore, a slight numerical oscillation of v can be admitted between x/H=0.9 and 1.0. Both of these aspects are due to the difference in the spatial discretization scheme between EMV and SMAC, i.e., SMAC employed the second-order central scheme for the advection term, whereas EMV inevitably adopted the first-order upwind scheme for the advection term in ρ equation and TVD scheme in u_i equations. This means that the artificial numerical viscosity was added only in the EMV to avoid numerical oscillation, which led to deviations between EMV and SMAC. As shown in Appendix A3, we confirmed that 2-D cavity flows using the first-order upwind deference scheme for both EMV and SMAC does not show any differences in velocity distributions, although the results are different from DNS data (Ghia 1982). These

12

371 results imply that EMV can reproduce the velocity fields similar to those in conventional
372 methods wherein the perfect incompressibility of fluid is assumed, although we have to
373 employ an appropriate advection scheme to avoid numerical oscillation and obtain converged
374 flow fields.
375   In contrast to these slight differences in EMV and SMAC, LBM shows larger
376 differences in both u and v. It should be noted that the discrepancies of EMV from SMAC
377 and DNS are much smaller than those of LBM, especially at $Re = 10000$.
378
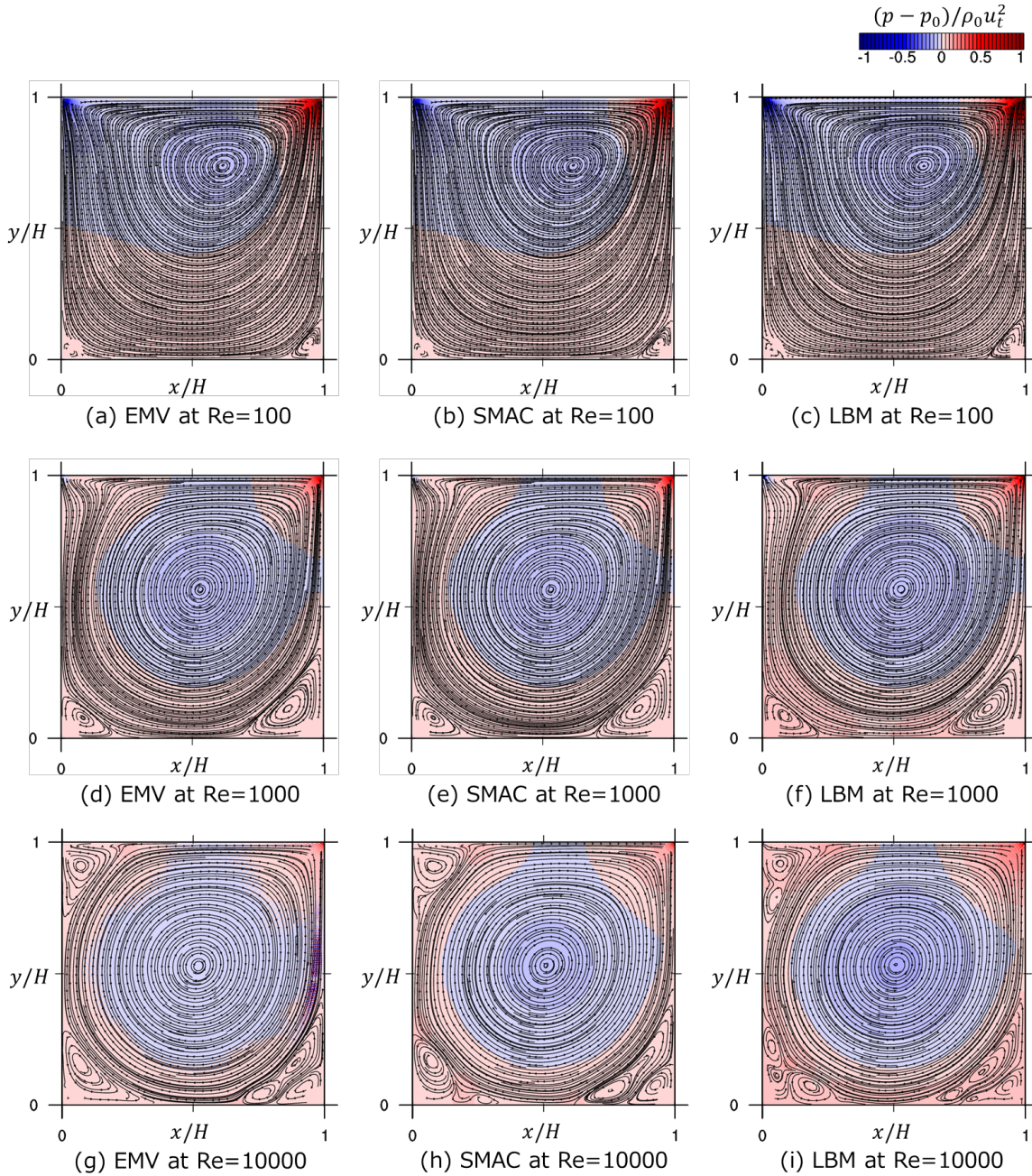
Fig.2 Streamlines and pressure distributions at each Reynolds number of (a-c) $Re = 100$,
(d-f) $Re = 1000$, and (g-i) Re=10000 at time, $t/t_e = 1$, where t_e is the duration when the
flow distribution converges. p_0 is the initial pressure value. The distributions are determined
by (a), (d), (c) EMV, (b), (e), (h) SMAC, and (c), (f), (i) LBM.

13

384

(a) Re=100
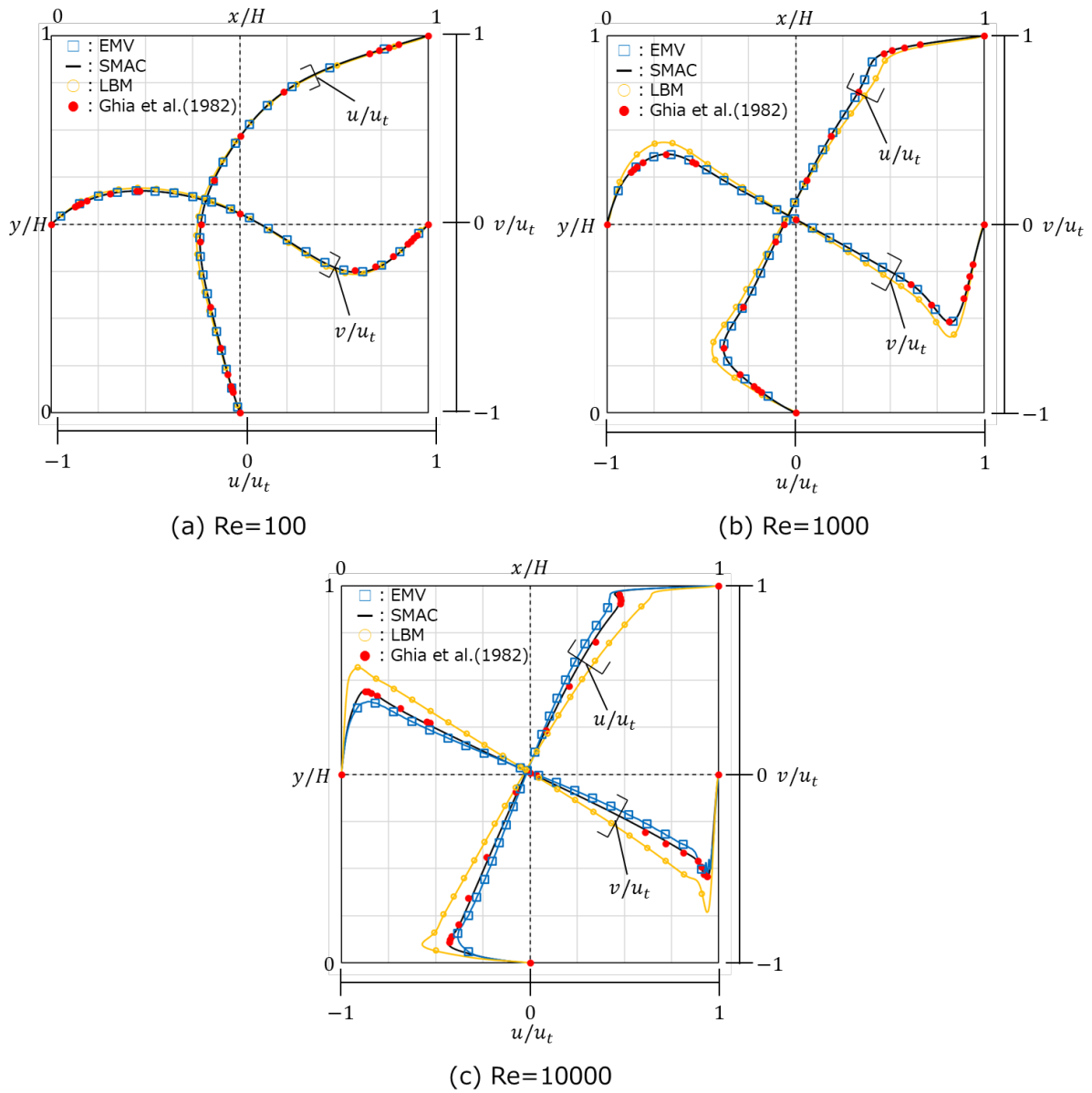
(b) Re=1000

(c) Re=10000

385
386 Fig.3 Velocity profiles in the center line of cavity for u at $x/H = 0.5$ and v at $y/H =$
387 0.5. (a) $Re = 100$, (b) $Re = 1000$, and (c) $Re = 10000$. Reference data is after Ghia et al.
388 (1982).

3.3. Temporal evolutions

The other concern is whether EMV can reproduce the temporal evolutions of the velocity fields consistent with the conventional method. In this section, we qualitatively discuss the temporal development of flow by comparing changes in the vortex structures within the cavity, and time evolutions of velocity at the center of the cavity.

Fig.4 shows the flow distributions determined by EMV and SMAC, $Re = 1000$ at three different moments of $t/t_e = 0.05$, 0.2, and 0.4 (The distributions at $Re = 100$ does not show significant difference between EMV and SMAC; therefore, we discuss the patterns of $Re = 1000$ and 10000). $t/t_e = 0.05$ in Figs. 4 (a) and (d), we can see the difference in streamlines at the bottom of the cavity, although the overall distribution patterns are similar to each other in terms of streamlines and locations of the primary vortex near $x/H = y/H \sim 0.8$. Additionally, the p distribution seems to show some difference. Such a difference may be due to the effect of acoustic wave propagating with the speed of sound. In SMAC, the assumption of incompressibility indicates that the propagating speed of acoustic wave is infinite, which is enabled by solving the Poisson equation of p. In contrast, the propagating speed in EMV is the artificial speed of sound $a = \Delta/\sqrt{3}\Delta t$ by solving the compressible continuity equation as explained in Section 2.3. Such differences become less significant as the time step evolves, as shown in Figs.4 (b) and (e), and Figs. 4 (c) and (f). At $t/t_e = 0.2$, the streamline and pressure distribution show good agreement except for the secondary vortex in the bottom-right corner of the cavity. Accordingly, the difference in flow patterns cannot be seen at $t/t_e = 0.4$.
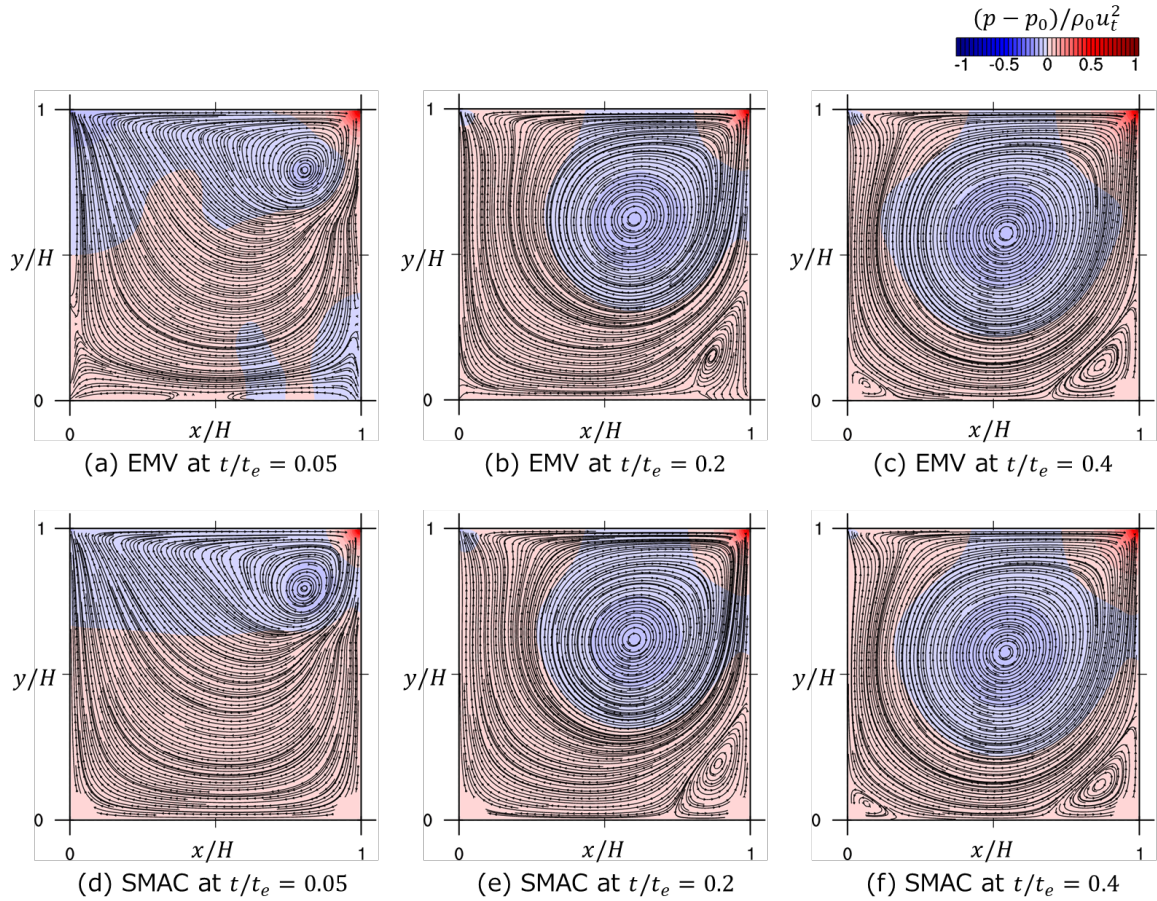
Fig. 5 looks the same as Fig. 4 but for $Re = 10000$. $t/t_e = 0.03$ in Figs. 5 (a) and (d), both results have two vortices near the center of the cavity; however, the shapes and locations of the two vortices differ in EMV and SMAC. Additionally, the secondary vortices observed near three corners of the cavity (i.e., $(x/H, y/H) \sim (0.1, 0.1)$, $(0.1, 0.9)$, and $(0.9, 0.1)$) show significant differences. For example, at $(0.1, 0.1)$, the core of the vortex is located at a lower and righter position for EMV than SMAC. With time development, these two vortices near the cavity center combine with each other and one primary vortex is formed at the center of the cavity, as seen in Figs. 5 (b) and (e). At this moment, the flow distributions are considerably similar in EMV and SMAC; however, slight differences can be observed near each corner. At $t/t_e = 0.2$ in Figs. 5 (c) and (f), the results of both EMV and SMAC are almost identical, although the numerical oscillations occur near the side wall, as seen in the profiles of v (in Fig. 3. (c)).

Figs. 6 and 7 show the temporal evolutions of u, v, and p at the center of the cavity ($x/H = 0.5$, $y/H = 0.5$), and the maximum and minimum density, ρ_{max} and ρ_{min}, within the entire domain at each time step to qualitatively discuss the differences in each method. The horizontal axis is normalized by t_e.
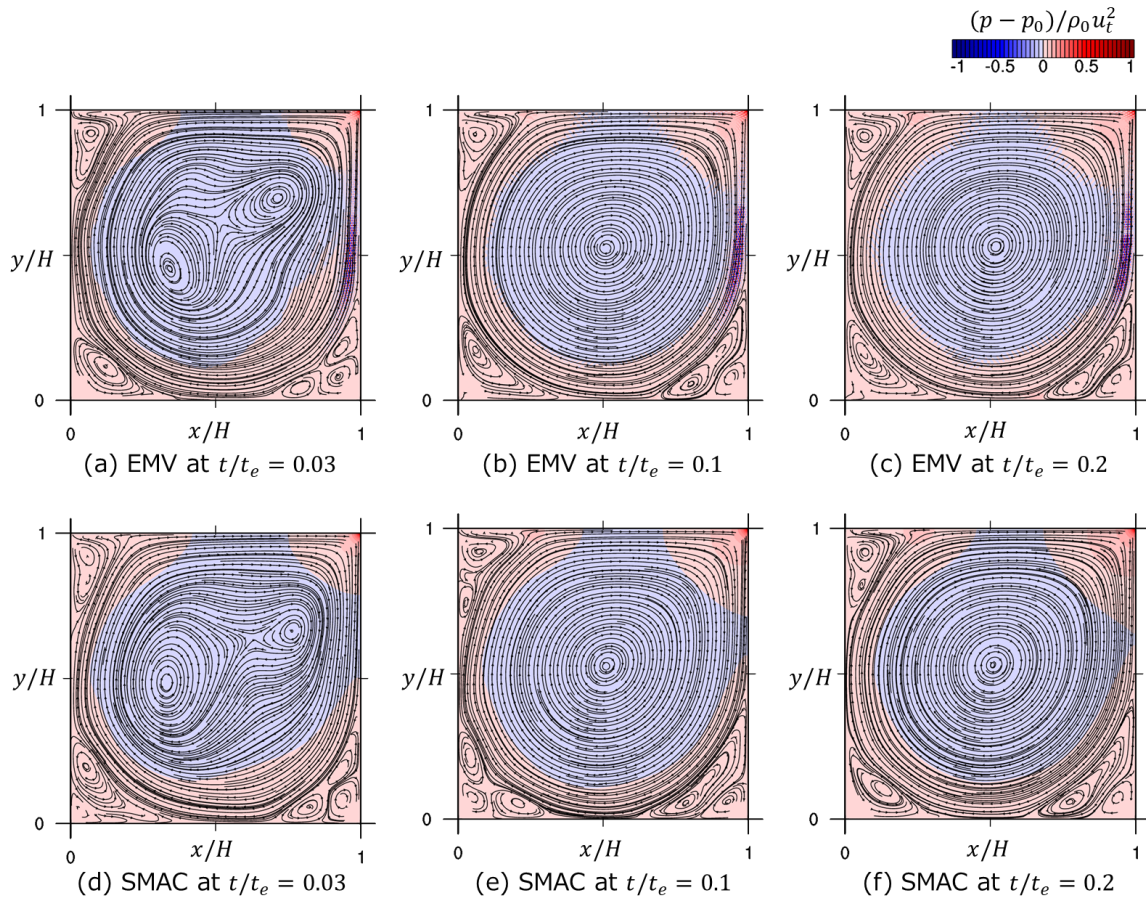
At $Re = 100$, both u and p by EMV show the apparent oscillation from $t/t_e = 0$ to 0.4, whereas those of SMAC do not fluctuate at all. Similar oscillations can be seen for the LBM. With temporal development, such oscillations decrease for EMV. Consequently, u, v, and p of the EMV agree well with those of the SMAC. These differences among the methods mean that the explicit method causes such oscillations with respect to time. However, we could not differentiate these oscillations from the numerical oscillation because they can occur due to the propagation of a wave with finite speed of sound. Additionally, we have to assume that the considerable smooth temporal development of velocity and p is unnatural owing to the iterative method while solving the Poisson equation of p in SMAC. Note that the difference in approached values of $t = t_e$ among EMV, SMAC, and LBM reflects the differences shown in profiles of Fig. 3. A similar trend can be seen when $Re = 1000$ in Figs.

15

437 6 (c) and (d). Regarding the compressible effect in EMV, Fig. 7 shows that the maximum
438 difference in the density is less than $\pm 5\%$.
439   Alternatively, Figs. 3 (e) and (f), $Re = 10000$ show that oscillations of u, v, and p of
440 EMV are not reduced even though time evolves. In contrast, those of SMAC show
441 significantly smooth changes with time. We cannot state that these fluctuations are artificial or
442 numerical problems; however, such fluctuations may cause the divergence of numerical
443 simulation and must be avoided for the numerically stable simulations. In addition, such
444 oscillations can also be seen in ρ_{max} and ρ_{min} of EMV (Fig. 7). However, the difference of
445 the density within the entire domain is kept less than 8% at $Re = 10000$.
446

$$(p - p_0)/\rho_0 u_t^2$$

(a) EMV at $t/t_e = 0.05$ (b) EMV at $t/t_e = 0.2$ (c) EMV at $t/t_e = 0.4$

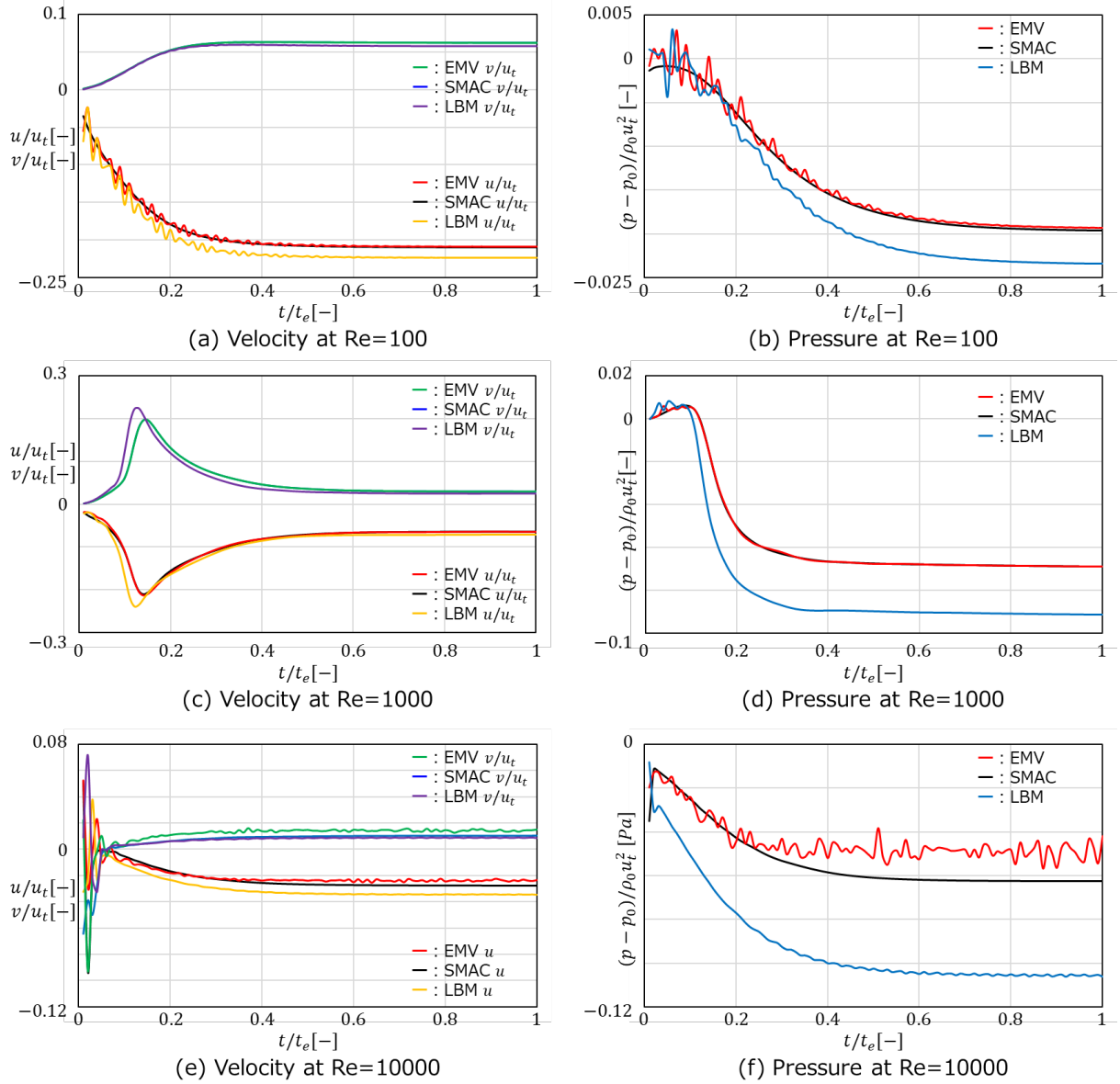(d) SMAC at $t/t_e = 0.05$ (e) SMAC at $t/t_e = 0.2$ (f) SMAC at $t/t_e = 0.4$

447
448 Fig.4 Temporal changes in velocity distributions for $Re = 1000$ for (a–c) EMV and (d–f)
449 SMAC. (a), (d) at $t/t_e = 0.05$, (b), (e), $t/t_e = 0.2$ and (c), (f) $t/t_e = 0.4$.
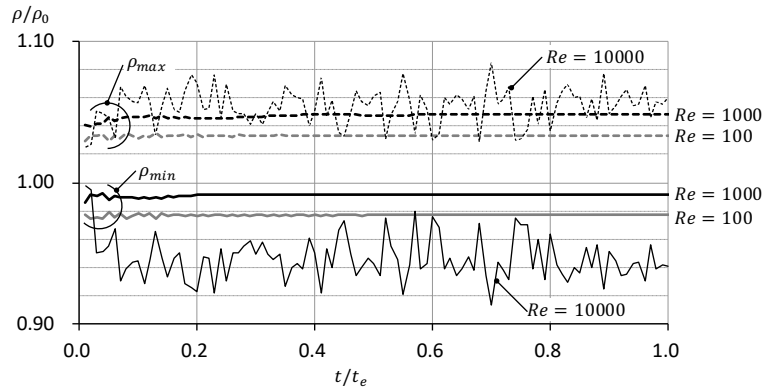
(a) EMV at $t/t_e = 0.03$ (b) EMV at $t/t_e = 0.1$ (c) EMV at $t/t_e = 0.2$

(d) SMAC at $t/t_e = 0.03$ (e) SMAC at $t/t_e = 0.1$ (f) SMAC at $t/t_e = 0.2$

450
451   Fig.5 Same as Fig. 4, but for $Re = 10000$. (a) (d) at $t/t_e = 0.03$, (b), (e), $t/t_e = 0.1$ and
452   (c), (f) $t/t_e = 0.2$.

(a) Velocity at Re=100

(b) Pressure at Re=100

(c) Velocity at Re=1000

(d) Pressure at Re=1000

(e) Velocity at Re=10000

(f) Pressure at Re=10000

Fig.6 Temporal evolutions of velocity and pressure at center of cavity ($x/H = 0.5$ and $y/H = 0.5$) for (a,b) $Re = 100$, (c,d) $Re = 1000$, and (e,f) $Re = 10000$.

Fig. 7 Temporal evolutions of maximum and minimum density, ρ_{max} and ρ_{min} within the entire domain at each time step. ρ_0 indicates the density at the initial condition.

18

4. Conclusion

In this paper, we discussed the theoretical interpretation of an artificially compressible method such as ACM and EDACM to propose a new explicit numerical method for numerical simulation of fluid flow. The new method, the explicit numerical method with virtual particle concept called as EMV, employs the compressible continuity and Navier–Stokes equations by replacing the pressure to density with an artificial parameter. Additionally, the validity of EMV was proven by comparing the results of the two-dimensional cavity flow among the conventional and reference numerical simulations.

In theoretical derivation, we confirmed that ACM and EDACM correspond to barotropic and isochoric conditions, respectively, by comparing the set of equations employed in ACM and EDACM with theoretically derived equations for the three macroscopic states. Previous studies have stated that ACM corresponds to the isentropic state; however, we extended the interpretation of ACM as a barotropic condition including both isothermal and isentropic states. Additionally, we provided a new interpretation of EDACM as the isochoric conditions. Moreover, we clarified the potential problems in artificial compressibility method: i) both ACM and EDACM may violate the mass conservation law under unsteady-state conditions, and ii) the governing equations of both methods cannot explain why artificial compressibility method can be employed with a as an arbitrary model parameter.

To overcome these problems, we propose a new simulation method called EMV, which employs compressible continuity and Navier–Stokes equations. By introducing the virtual particle concept, we provide a theoretical interpretation of replacing a as an artificial parameter determined by the grid system of numerical simulation.

To confirm the validity of EMV, a numerical simulation of two-dimensional cavity flow was compared with EMV, SMAC, LBM, and previous numerical simulations for three conditions of $Re = 100,\ 1000,$ and 10000. The results of EMV agree well with SMAC and reference data for both steady-state and temporal evolutions in comparison with those of LBM at $Re = 100$ and 1000. In contrast, when $Re = 10000$, the numerical oscillation could be seen only in the EMV results. Hence we conclude that such oscillations are due to the numerical instability of the advection term, which can be avoided by applying a numerically suitable scheme even in EMV.

Although the proposed method was verified in terms of theoretical framework with the virtual particle concept as well as numerical feasibility, comparable with previous methods, our numerical simulations employed in this study were very simple for two-dimensional cavity flow. Furthermore, we only employed the staggered grid system by using SMAC and EMV methods. The proposed method will be adopted for various flows with difference grid systems in future studies, yielding the development of an explicit method for numerically efficient simulation.

19

505 Appendix
506 A1. Distribution function of a virtual particle
507   The distribution function of molecules is expressed by the Maxwell distribution as
508 follows:

$$f(\boldsymbol{q}) = \left(\frac{m\beta}{2\pi}\right)^{\frac{3}{2}} exp\left(-\frac{m\beta}{2}\boldsymbol{q}^2\right). \tag{A1.1}$$

509 Here, $\boldsymbol{q}$ and m represent the velocity and mass of molecules, $\beta = 1/k_B T$ is the inverse
510 temperature, and k_B is the Boltzmann constant. When all the molecules are exposed to a
511 macroscopic velocity $\boldsymbol{u}$, the distribution is modified as

$$f(\boldsymbol{q}) = \left(\frac{m\beta}{2\pi}\right)^{\frac{3}{2}} exp\left(-\frac{m\beta}{2}(\boldsymbol{q}-\boldsymbol{u})^2\right), \tag{A1.2}$$

512 because the relative velocity of molecules becomes $\boldsymbol{q} - \boldsymbol{u}$.
513   We assume that the distribution function of virtual particles, f_i, can be expressed by
514 a similar function by applying the Taylor series expansion up to $\boldsymbol{u}^2$:

$$f_i = A_i[1 + B\boldsymbol{u}\cdot\boldsymbol{u} - 2B\boldsymbol{c}_i\cdot\boldsymbol{u} + 2B^2(\boldsymbol{c}_i\cdot\boldsymbol{u})^2]. \tag{A1.3}$$

515 Here, A_i ($i = 0$ to M, where M is the number of velocities in a lattice grid) and $B =$
516 $-3/2c^2$ ($c = \Delta/\Delta t$, where is the representative speed of virtual particles defined by the
517 shortest grid length Δ and the representative time scale Δt) are determined to satisfy the
518 macroscopic nature of a fluid, independently. The ultra-discretized velocity is denoted as $\boldsymbol{c}_i$
519 ($i = 0$ to M). A_i and $\boldsymbol{c}_i$ are determined once a lattice grid on which the virtual particles
520 can move is selected. If we employ the typical velocity and lattice grid models used in the
521 Lattice–Boltzmann method, as shown in Fig. A1, we can obtain these coefficients, as listed in
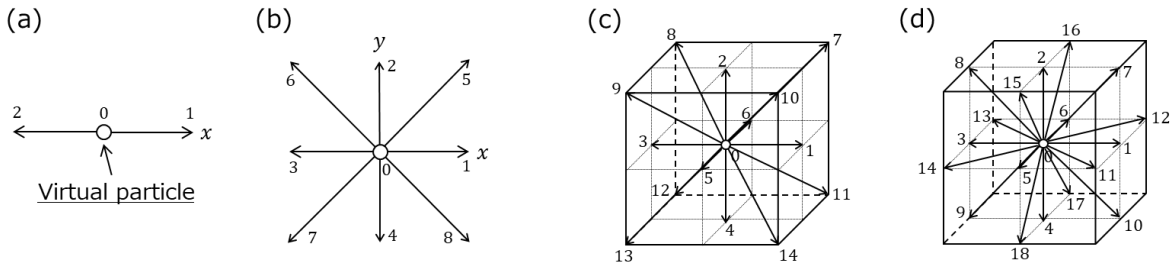522 Table A1.
523   By using these coefficients, q_{vT} is explicitly determined as

$$q_{vT} = \Sigma_i f_i \boldsymbol{c}_i^2 = \frac{D}{3}c^2, \tag{A1.4}$$

524 regardless of the selection of the lattice grid. This also gives the simplest form of p_v as

$$p_v = \rho\frac{c^2}{3} = \frac{\rho}{3}\left(\frac{\Delta}{\Delta t}\right)^2. \tag{A1.5}$$

525

526
527 Fig. A1 Definition of lattice grids (a) 1D3V, (b) 2D9V, (c) 3D15V, and (d) 3D19V models
528
529 Table A1: Coefficient for the discrete distribution function f_i. For 1D3V, $C_1 = A_0$ and $C_2 = $
530 $A_1 = A_2$, for 2D9V, $C_1 = A_0$, $C_2 = A_1$ to A_4, and $C_3 = A_5$ to A_8, for 3D15, $C_1 = A_0$,
531 $C_2 = A_1$ to A_6, and $C_3 = A_7$ to A_{14}, and for 3D19V, $C_1 = A_0$, $C_2 = A_1$ to A_6, and $C_3 = $
532 A_7 to A_{18}.

Lattice grid types	C_1	C_2	C_3
1D3V	2/3	1/6	-
2D9V	4/9	1/9	1/36
3D15V	2/9	1/9	1/72
3D19V	1/3	1/18	1/36

533

534

A2. Discretization

For two-dimensional cavity flow of compressible fluids, the governing equations with virtual particle concepts can be written as follows:

$$\frac{\partial \rho}{\partial t} + \frac{\partial \rho u}{\partial x} + \frac{\partial \rho v}{\partial y} = 0, \tag{A2.1}$$

$$\frac{\partial \rho u}{\partial t} + \frac{\partial \rho u^2}{\partial x} + \frac{\partial \rho u v}{\partial y} = -\frac{c^2}{3}\frac{\partial \rho}{\partial x} + \mu \frac{\partial^2 u}{\partial x^2} + \mu \frac{\partial^2 u}{\partial y^2}, \tag{A2.2}$$

$$\frac{\partial \rho v}{\partial t} + \frac{\partial \rho u v}{\partial x} + \frac{\partial \rho v^2}{\partial y} = -\frac{c^2}{3}\frac{\partial \rho}{\partial y} + \mu \frac{\partial^2 v}{\partial x^2} + \mu \frac{\partial^2 v}{\partial y^2}. \tag{A2.3}$$

By replacing the pressure term with ρ and $c = \Delta/\Delta t$ based on the virtual particle concept, the first equation obtained is the continuity, and the latter two are Navier–Stokes (NS) equations. The second viscosity terms in NS equations do not appear in two-dimensional cases because $\lambda = -\mu$. The variables are defined at each stencil based on staggered grids. The velocity u, v, and density ρ are defined at (i,J), (I,j) and (I,J) as shown in Fig. A1. These variables are denoted as, u_{iJ}, v_{Ij}, and ρ_{IJ}. When a quantity that is not defined at the grids is required, the values are interpolated by variables defined on the grids. The interpolation method is explained in each budget equation.

The discrete form of continuity is derived by following the finite volume method as

$$\int_{V_{IJ}} \frac{\partial \rho}{\partial t} dV + \int_{V_{IJ}} \left(\frac{\partial \rho u}{\partial x} + \frac{\partial \rho v}{\partial y} \right) dV = 0. \tag{A2.4}$$

By taking the average volume with respect to the cell V_{IJ} for $\rho_P = \rho_{IJ}$ (Fig. A2), where the subscript P indicates the present position when volume is considered. By employing first-order Euler discretization method for storage term and defining the numerical flux at the boundary b (=e, w, s, and n), ϕ_b^*, Eq. (A2.4) is written as

$$\rho_{I,J}^{n+1} = \rho_P - \frac{\Delta}{a_O}(\phi_e^* u_e - \phi_w^* u_w + \phi_n^* v_n - \phi_s^* v_s), \tag{A2.5}$$

where, $u_e = u_{i+1,J}$, $u_w = u_{i,J}$, $v_n = v_{I,j+1}$, $v_s = v_{I,j}$, and $a_O = \Delta^2/\Delta t$. The superscript $n + 1$ represents the value at time step $n + 1$. The variables without the superscript indicate the value at the time step of n. ϕ_b^* is defined as a general numerical flux form by employing a parameter ψ as

$$\phi_b^* = \phi_U + 0.5\psi(\phi_D - \phi_U). \tag{A2.6}$$

Here, the subscripts U and D indicate the quantities at the upwind and downwind stencils with respect to b in Fig. A1 (b). ϕ_b^* can be written in a form consistent with the central interpolation schemes as

$$\phi_b^* = 0.5(\phi_U + \phi_D) + 0.5(1 - \psi)(\phi_U - \phi_D). \tag{A2.7}$$

ψ can be used to control the numerical viscosity to avoid numerical oscillation. $\psi = 0$ and $\psi = 1$ correspond to upwind and central interpolation schemes, respectively. The total variation diminishing (TVD) scheme requires ψ to be in TVD region as a function of the local gradient r_b. An example of $\psi(r_b)$ is the van Albada limiter function [22], as used in this paper.

$$\psi(r_b) = \frac{r_b + r_b{}^2}{1 + r_b{}^2}, \tag{A2.8}$$

$$r_b = \frac{\phi_U - \phi_{UU}}{\phi_D - \phi_U}. \tag{A2.9}$$

Here, the superscript UU indicates the two-grid upwind stencil with respect to b in Fig. A2(b).

By substituting Eq. (A2.7) in Eq. (A2.5), the discrete continuity equation can be written as the form consistent with the central interpolated scheme as

21

$$\rho_{I,J}^{n+1} = \left(1 + \frac{a_P - b_P}{a_O}\right)\rho_P + \Sigma_M \frac{a_M + b_M}{a_O}\rho_M. \tag{A2.10}$$

567 Here, the coefficients are defined as follows: $a_E = -0.5u_e\Delta$, $a_W = 0.5u_w\Delta$, $a_N = -0.5v_n\Delta$,
568 $a_S = 0.5v_s\Delta$, $b_E = 0.5\big(1 - \psi(r_e)\big)|u_e|\Delta$, $b_W = 0.5\big(1 - \psi(r_w)\big)|u_w|\Delta$, $b_N = 0.5\big(1 -$
569 $\psi(r_n)\big)|v_n|\Delta$, $b_S = 0.5\big(1 - \psi(r_s)\big)|v_s|\Delta$, $a_P = \Sigma_M a_M$ and $b_P = \Sigma_M b_M$. Σ_M means taking all
570 summation with respect to the surrounding stencils of $M = E, W, N$ and S (Fig. A2 (b)).
571   Similarly, the momentum equation of u can be integrated with respect to the volume
572 $V_{i,J}$ for $u_P = u_{i,J}$ as

$$\int_{V_{i,J}} \frac{\partial\rho u}{\partial t}dV + \int_{V_{i,J}} \left(\frac{\partial\rho u^2}{\partial x} + \frac{\partial\rho uv}{\partial y}\right)dV = -\frac{c^2}{3}\int_{V_{i,J}} \frac{\partial\rho}{\partial x}dV + \int_{V_{i,J}} \left(\mu\frac{\partial^2 u}{\partial x^2} + \mu\frac{\partial^2 u}{\partial y^2}\right)dV. \tag{A2.11}$$

573 By employing the first-order Euler scheme for storage, the central interpolation scheme for
574 diffusion terms, and the numerical flux in the advection terms, the discrete form can be
575 written as follows:

$$u_P^{n+1} = \left(\frac{\rho_P}{\rho_P^{n+1}} - \frac{c_P}{c_O\rho_P^{n+1}}\right)u_P - \frac{c^2\Delta}{3c_O\rho_P^{n+1}}(\rho_e^{n+1} - \rho_w^{n+1}) + \frac{1}{c_O\rho_P^{n+1}}\Sigma_M c_M u_M$$
$$+ \frac{\Delta}{c_O\rho_P^{n+1}}(\rho_e\phi_e^* - \rho_w\phi_w^* + v_n\phi_n^* - v_s\phi_s^*). \tag{A2.12}$$

576 Here, $\rho_e = \rho_{I,J}$, $\rho_w = \rho_{I-1,J}$, $\rho_e^{n+1} = \rho_{I,J}^{n+1}$, $\rho_w^{n+1} = \rho_{I-1,J}^{n+1}$, $\rho_P = 0.5(\rho_e + \rho_w)$, $\rho_P^{n+1} =$
577 $0.5(\rho_e^{n+1} + \rho_w^{n+1})$, $v_n = 0.5(v_{I,j+1} + v_{I-1,j+1})$, $v_s = 0.5(v_{I,j} + v_{I-1,j})$. The coefficients are
578 defined as follows: $c_O = \Delta t/\Delta^2$, $c_E = c_W = c_N = c_S = \mu$, $c_P = \Sigma_M c_M$. ϕ_e^* and ϕ_w^*, and,
579 ϕ_n^* and ϕ_s^*, are determined by taking $\phi = u^2$ and $\phi = \rho u$ in Eq. (A2.6), respectively.
580 ρ_P^{n+1} is taken at $n+1$ time step, for consistency of the discrete form for $\partial\rho u/\partial t$ and
581 $u\partial\rho\partial t + \rho\partial u/\partial t$. Moreover, the densities in term $\partial\rho/\partial x$ are determined by the values at
582 $n+1$ time step using Eq. (A2.10), which is solved before the momentum equations because
583 of the convergence of Eq. (A2.12).
584   In the same matter, the momentum equation of v can be integrated with respect to
585 the volume $V_{I,j}$, and the following equation can be obtained.

$$v_P^{n+1} = \left(\frac{\rho_P}{\rho_P^{n+1}} - \frac{d_P}{d_O\rho_P^{n+1}}\right)v_P - \frac{c^2\Delta}{3d_O\rho_P^{n+1}}(\rho_n^{n+1} - \rho_s^{n+1}) + \frac{1}{d_O\rho_P^{n+1}}\Sigma_M d_M u_M$$
$$+ \frac{\Delta}{d_O\rho_P^{n+1}}(u_e\phi_e^* - u_w\phi_w^* + \rho_n\phi_n^* - \rho_s\phi_s^*). \tag{A2.13}$$

586 Here, $\rho_n = \rho_{I,J}$, $\rho_s = \rho_{I,J-1}$, $\rho_n^{n+1} = \rho_{I,J}^{n+1}$, $\rho_s^{n+1} = \rho_{I,J-1}^{n+1}$, $\rho_P = 0.5(\rho_n + \rho_s)$, $\rho_P^{n+1} =$
587 $0.5(\rho_n^{n+1} + \rho_s^{n+1})$, $u_e = 0.5(u_{i+1,J} + u_{i+1,J-1})$, $u_w = 0.5(u_{i,J} + u_{i,J-1})$. The coefficients
588 are defined as follows: $d_O = \Delta t/\Delta^2$, $d_E = d_W = d_N = d_S = \mu$, $d_P = \Sigma_M d_M$. ϕ_e^* and ϕ_w^*,
589 and, ϕ_n^* and ϕ_s^*, are determined by taking $\phi = \rho v$ and $\phi = v^2$ in Eq. (A2.6), respectively.
590   When the numerical flux at boundary b can be estimated by each interpolated value
591 at b, Eqs. (A2.12) and (A2.13) can be written in a form consistent with the central
592 interpolated schemes as follows:

$$u_P^{n+1} = \left(\frac{\rho_P}{\rho_P^{n+1}} + \frac{f_P - c_P - g_P}{c_O\rho_P^{n+1}}\right)u_P - \frac{c^2\Delta}{3c_O\rho_P^{n+1}}(\rho_e^{n+1} - \rho_w^{n+1}) + \Sigma_M \frac{c_M + 0.5f_M + g_M}{c_O\rho_P^{n+1}}u_M, \tag{A2.14}$$

$$v_P^{n+1} = \left(\frac{\rho_P}{\rho_P^{n+1}} + \frac{h_P - d_P - k_p}{d_O\rho_P^{n+1}}\right)v_P - \frac{c^2\Delta}{3d_O\rho_P^{n+1}}(\rho_n^{n+1} - \rho_s^{n+1}) + \Sigma_M \frac{d_M + 0.5h_M + k_M}{d_O\rho_P^{n+1}}v_M. \tag{A2.15}$$

593 Here, the additional coefficients are defined as follows: $f_E = -\rho_e\phi_e^*\Delta$, $f_W = \rho_w\phi_w^*\Delta$, $f_N =$
594 $-v_n\phi_e^*\Delta$, $f_S = v_s\phi_s^*\Delta$, $f_P = \Sigma_M f_M$. ϕ_e^* and ϕ_w^* are interpolated values using Eq. (A2.6)
595 with $\phi = u$, and ϕ_n^* and ϕ_s^* are interpolated values using Eq. (A2.6) with $\phi = \rho$. $g_B =$
596 $0.5|f_B|(1 - \psi(r_b))$ for $B = E, W, N$ and S, $g_P = \Sigma_M g_M$. Similarly, $h_E = -u_e\phi_e^*\Delta$,
597 $h_W = u_w\phi_w^*\Delta$, $h_N = -\rho_n\phi_e^*\Delta$, $h_S = \rho_s\phi_s^*\Delta$, $h_P = \Sigma_M h_M$. ϕ_e^* and ϕ_w^* are interpolated

598 values by Eq. (A2.6) with $\phi = \rho$, and ϕ_n^* and ϕ_s^* are interpolated values using Eq. (A2.6)
599 with $\phi = v$. $k_B = 0.5|h_B|(1 - \psi(r_b))$ for $= E, W, N$ and S, $k_P = \Sigma_M k_M$.
600
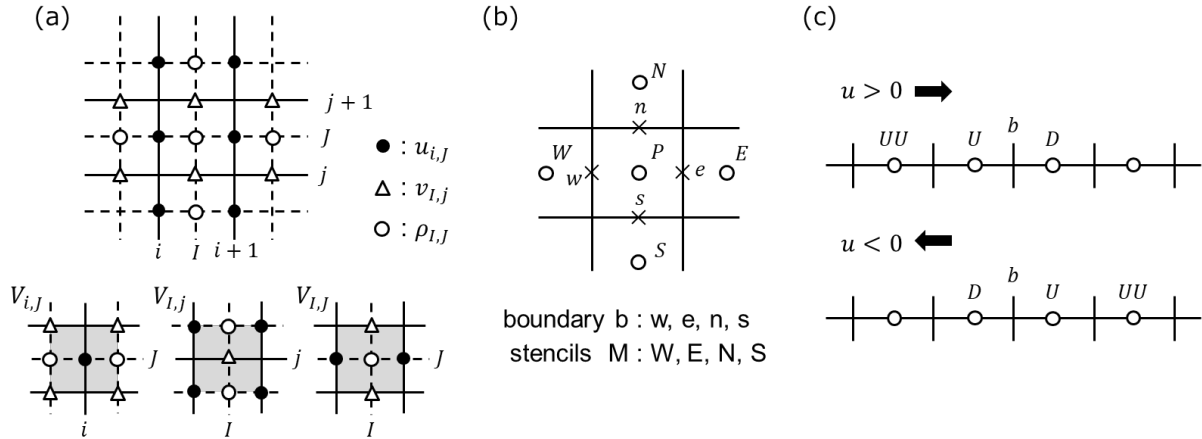
601
602 Fig.A2 Grid definition. (a) variables on the staggered grid and control volume V_{IJ}, V_{iJ}, and
603 V_{Ij}, (b) boundary b (=w, e, s, and n) and stencils M (=W, E, S, and N), and (c) stencils
604 of UU, U, and D with respect to the boundary b for the TVD scheme.
605

606 A.3 Comparisons between EMV and SMAC with upwind scheme
607   In Section 3, we clarified that EMV and SMAC showed slight differences in the
608 velocity fields at $Re = 10000$. This is because of the difference in the numerical scheme for
609 discretization of the advection term, but is not due to the proposed method where $a =$
610 $\Delta/\sqrt{3}\Delta t$. To confirm this aspect, the results are presented here by applying the first-order
611 upwind scheme in both continuity and N-S equations for EMV and SMAC.
612   Fig. A3 shows the snapshots at $t = t_e$. Clearly, the locations of each vortex core and
613 the size of the primary and secondary vortices are consistent between EMV and SMAC. Fig.
614 A4 shows the velocity profiles at $x/H = 0.5$ for u at $y/H = 0.5$ for v. These profiles
615 considerably agree between EMV and SMAC, including near each wall where the velocity
616 shear becomes significant. Fig. A5 shows the temporal evolutions of velocity and pressure at
617 the center of cavity ($x/H = 0.5$ and $y/H = 0.5$). The time evolutions between the two
618 methods show good agreement. Alternatively, the velocity and pressure field simulated by the
619 first-order upwind scheme are considerably different from those simulated by the SMAC with
620 second-order scheme or previous results by Ghia (1982), as shown in Figs. A4 and A5.
621 According to these results, we can conclude that the idea employed in EMV is acceptable for
622 reproducing the velocity and pressure field consistent with those by SMAC. However, we
623 need to consider an appropriate discretization scheme for the advection term due to numerical
624 instability in the explicit numerical simulations.
625

(a) EMV at Re=10000   (b) SMAC at Re=10000
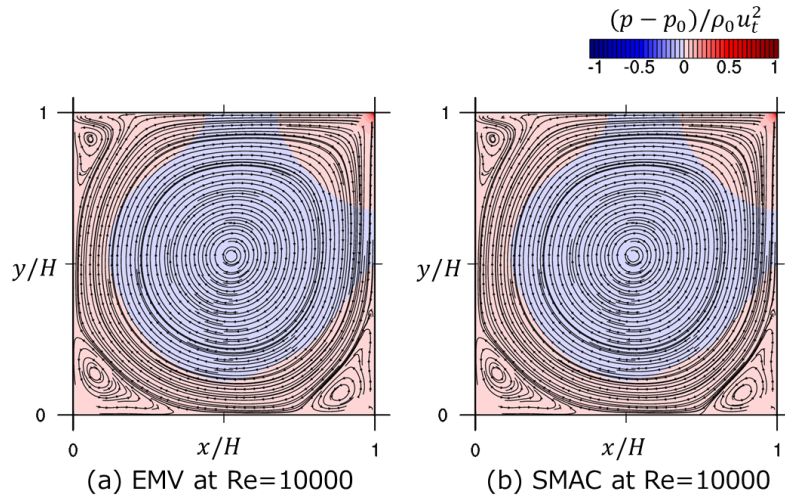
Fig. A3 Streamlines and pressure distributions at $Re = 10000$ for (a) EMV and (b) SMAC with first-order upwind advection scheme for advection term.
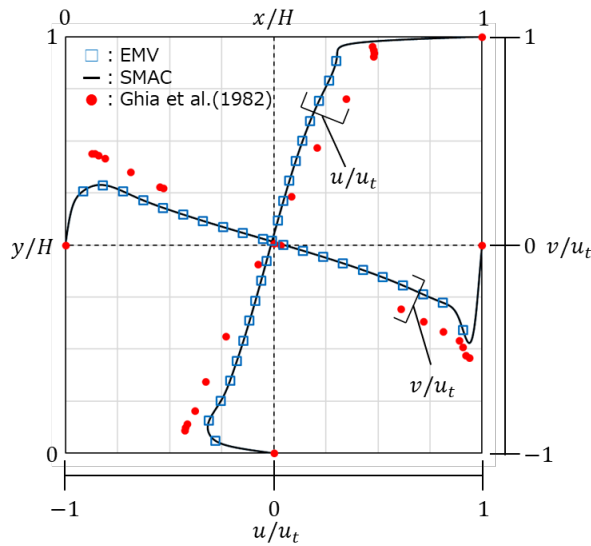
Fig. A4 Velocity profiles in the center lines of cavity for u at $x/H = 0.5$ and v at $y/H = 0.5$. for $Re = 10000$ with the first-order upwind scheme for the advection term. Reference data is after Ghia et al. (1982).
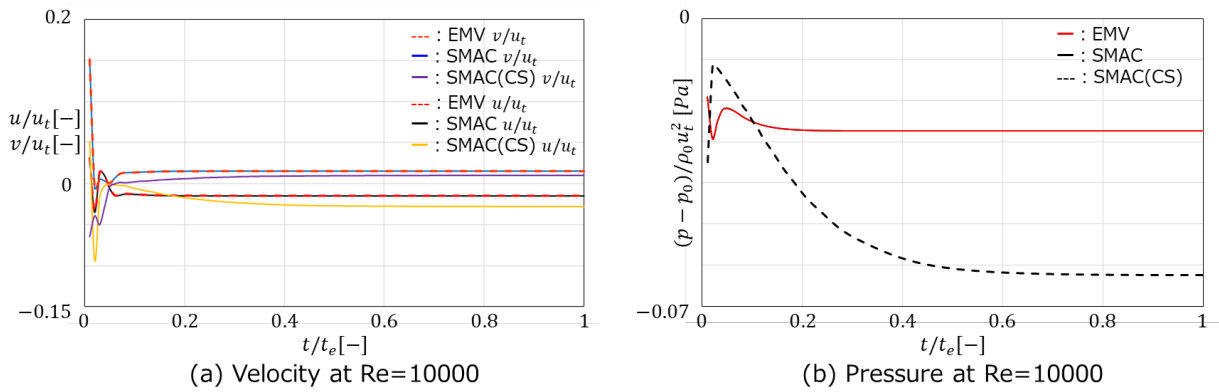
(a) Velocity at Re=10000   (b) Pressure at Re=10000

636   Fig. A5 Temporal evolutions of (a) velocity and (b) pressure at center of cavity ($x/H = 0.5$
637   and $y/H = 0.5$) for $Re = 10000$ with the first-order upwind scheme. CS is the
638   second-order center scheme used for SMAC in Section 3.

639   Nomenclature:
640    $a = (dp/d\rho)^{0.5}$: speed of sound [m/s]
641    $c = \Delta/\Delta t$: representative speed of virtual particle [m/s]
642    $\boldsymbol{c}_i$: ultra-discrete velocity of virtual particle [m/s]
643   c_p: specific heat under isobar condition [J/kgK]
644   c_v: specific heat under isochoric condition [J/kgK]
645   D: dimension [-]
646    $e_{ij} = (\partial u_i/\partial x_j + \partial u_j/\partial x_i)$: velocity strain tensor [1/s]
647   k: thermal conductivity [J/Kms]
648   k_B: Boltzmann constant [J/K]
649   m: mass of molecule [kg/pcs]
650   N: molecule density per unit volume [pcs/m^3]
651   n: amount of substance [mol]
652   N_A: Avogadro number [-]
653   p: pressure [Pa]
654   p_v: pressure by virtual particle impulse [Pa]
655    $\boldsymbol{q}^i$: velocity of molecule i [m/s]
656    $q_x^i, q_y^i,\ q_z^i$: velocity component of molecule i [m/s]
657   q_T: thermal velocity [m/s]
658    $\boldsymbol{q}_v^i$: velocity of virtual particle i [m/s]
659    $q_{v_x}^i, q_{v_y}^i,\ q_{v_z}^i$: velocity component of molecule i [m/s]
660   q_{v_T}: thermal velocity defined by virtual particle [m/s]
661   R: gas constant [J/kgK] ($p/\rho = RT$: ideal gas law)
662   s: specific entropy [J/kgK]
663   T: temperature [K]
664   t: time [s]
665   U: internal energy [J]
666   U_v: internal energy by virtual particle [J]
667   u_i: velocity in tensor notation [m/s]
668   V: fluid velocity [m/s]
669    $u,\ v,\ w$: velocity in component notation [m/s]
670    $x,\ y,\ z$: coordinate in component notation [m]
671   x_i: coordinate [m]
672    $\alpha = k/\rho c_p$: thermal diffusivity [m^2/s]
673    $\gamma = c_p/c_v$: ratio of specific heat [−]
674   Δ: grid spacing [m]
675   Δt: discrete time [s]
676   δ_{ij}: Kronecker's delta [-]
677    $\theta = \partial u_i/\partial x_i$: divergence of u_i [1/s]
678   λ: second dynamic viscosity [kg/ms]
679   μ: dynamic viscosity [kg/ms]
680   ϕ: dissipation rate [J/m^{3}s]
681    $\rho,\ \rho_0,\ \rho_{max},\ \rho_{min}$: density [kg/m^3]
682   Ω: volume [m^3]

683   Reference:

684   [1]   A.J. Chorin, A numerical method for solving incompressible viscous flow problems, J.
685   Comput. Phys. 2 (1967) 12–26. https://doi.org/10.1016/0021-9991(67)90037-X.

686   [2]   J.L. Steger, P. Kutler, Implicit Finite-Difference Procedures for the Computation of
687   Vortex Wakes, AIAA J. 15 (1977) 581–590. https://doi.org/10.2514/3.60663.

688   [3]   P.A. Madsen, H.A. Schäffer, A discussion of artificial compressibility, Coast. Eng. 53
689   (2006) 93–98. https://doi.org/10.1016/j.coastaleng.2005.09.020.

690   [4]   S. Vrahliotis, T. Pappou, S. Tsangaris, Artificial compressibility 3-D Navier-Stokes
691   solver for unsteady incompressible flows with hybrid grids, Eng. Appl. Comput. Fluid
692   Mech. 6 (2012) 248–270. https://doi.org/10.1080/19942060.2012.11015419.

693   [5]   J.R. Clausen, Entropically damped form of artificial compressibility for explicit
694   simulation of incompressible flow, Phys. Rev. E - Stat. Nonlinear, Soft Matter Phys. 87
695   (2013) 1–12. https://doi.org/10.1103/PhysRevE.87.013309.

696   [6]   S. Ansumali, I. V. Karlin, H.C. Öttinger, Thermodynamic theory of incompressible
697   hydrodynamics, Phys. Rev. Lett. 94 (2005) 1–4.
698   https://doi.org/10.1103/PhysRevLett.94.080602.

699   [7]   S. Borok, S. Ansumali, I. V. Karlin, Kinetically reduced local Navier-Stokes equations
700   for simulation of incompressible viscous flows, Phys. Rev. E - Stat. Nonlinear, Soft
701   Matter Phys. 76 (2007) 1–9. https://doi.org/10.1103/PhysRevE.76.066704.

702   [8]   A. Toutant, General and exact pressure evolution equation, Phys. Lett. Sect. A Gen. At.
703   Solid State Phys. 381 (2017) 3739–3742.
704   https://doi.org/10.1016/j.physleta.2017.10.008.

705   [9]   A. Toutant, Numerical simulations of unsteady viscous incompressible flows using
706   general pressure equation, J. Comput. Phys. 374 (2018) 822–842.
707   https://doi.org/10.1016/j.jcp.2018.07.058.

708   [10]   P. Bigay, G. Oger, P.M. Guilcher, D. Le Touzé, A weakly-compressible Cartesian grid
709   approach for hydrodynamic flows, Comput. Phys. Commun. 220 (2017) 31–43.
710   https://doi.org/10.1016/j.cpc.2017.06.010.

711   [11]   U. Frisch, D. D'humieres, B. Hasslacher, P. Lallemand, Y. Ves Pomeau, J.-P.R. Ivet,
712   Lattice Gas Hydrodynamics in Two and Three Dimensions, Complex Syst. 1 (1987)
713   649–707.

714   [12]   X. He, G.D. Doolen, T. Clark, Comparison of the lattice Boltzmann method and the
715   artificial compressibility method for Navier-Stokes equations, J. Comput. Phys. 179
716   (2002) 439–451. https://doi.org/10.1006/jcph.2002.7064.

717   [13]   J.D. Ramshaw, V.A. Mousseau, Accelerated artificial compressibility method for
718   steady-state incompressible flow calculations, Comput. Fluids. 18 (1990) 361–367.
719   https://doi.org/10.1016/0045-7930(90)90027-U.

720   [14]   Y.T. Delorme, K. Puri, J. Nordstrom, V. Linders, S. Dong, S.H. Frankel, A simple and
721   efficient incompressible Navier–Stokes solver for unsteady complex geometry flows
722   on truncated domains, Comput. Fluids. 150 (2017) 84–94.
723   https://doi.org/10.1016/j.compfluid.2017.03.030.

724   [15]   A. Kajzer, J. Pozorski, Application of the Entropically Damped Artificial
725   Compressibility model to direct numerical simulation of turbulent channel flow,
726   Comput. Math. with Appl. 76 (2018) 997–1013.
727   https://doi.org/10.1016/j.camwa.2018.05.036.

728   [16]   T. Ohwada, P. Asinari, Artificial compressibility method revisited: Asymptotic
729   numerical method for incompressible Navier-Stokes equations, J. Comput. Phys. 229
730   (2010) 1698–1723. https://doi.org/10.1016/j.jcp.2009.11.003.

731   [17]   A. Kajzer, J. Pozorski, A weakly Compressible, Diffuse-Interface Model for

732   Two-Phase Flows, Springer Netherlands, 2020.
733   https://doi.org/10.1007/s10494-020-00164-8.
734 [18] A.A. Amsden, F.H. Harlow, A simplified MAC technique for incompressible fluid
735   flow calculations, J. Comput. Phys. 6 (1970) 322–325.
736   https://doi.org/10.1016/0021-9991(70)90029-X.
737 [19] U. Ghia, K.N. Ghia, C.T. Shin, High-Re solutions for incompressible flow using the
738   Navier-Stokes equations and a multigrid method, J. Comput. Phys. 48 (1982) 387–411.
739   https://doi.org/10.1016/0021-9991(82)90058-4.
740 [20] S.G. Rubin, P.K. Khosla, Navier-Stokes calculations with a coupled strongly implicit
741   method-I. Finite-difference solutions, Comput. Fluids. 9 (1981) 163–180.
742   https://doi.org/10.1016/0045-7930(81)90023-2.
743 [21] F.H. Harlow, J.E. Welch, Numerical calculation of time-dependent viscous
744   incompressible flow of fluid with free surface, Phys. Fluids. 8 (1965) 2182–2189.
745   https://doi.org/10.1063/1.1761178.
746 [22] G.D. van Albada, B. van Leer, W.W. Roberts, A Comparative Study of Computational
747   Methods in Cosmic Gas Dynamics, Upwind and High-Resolution Schemes. 108 (1997)
748   95–103. https://doi.org/10.1007/978-3-642-60543-7_6.
749 [23] S. Chen, H. Chen, D. Martnez, W. Matthaeus, Lattice Boltzmann model for simulation
750   of magnetohydrodynamics, Phys. Rev. Lett. 67 (1991) 3776–3779.
751   https://doi.org/10.1103/PhysRevLett.67.3776.
752 [24] P.K. Khosla, S.G. Rubin, A diagonally dominant second-order accurate implicit
753   scheme, Comput. Fluids. 2 (1974) 207–209.
754   https://doi.org/10.1016/0045-7930(74)90014-0.